Article

Model Amphiphilic Polymer Conetworks in the Bulk: Dissipative Particle Dynamics Simulations of Their Self-Assembly and Mechanical Properties

Dimitrios G. Tsalikis, Mihai Ciobanu, Costas S. Patrickios,* and Yuji Higuchi

Read Online

ACCESS | Metrics & More | Article Recommendations | SI Supporting Information

ABSTRACT: Dissipative particle dynamics (DPD) simulations were performed on bulk melts of model amphiphilic polymer conetworks (APCN), a relatively new macromolecular architecture comprising two types of mutually incompatible polymer segments, and provided their morphological behavior and mechanical properties under uniaxial elongation. The simulated APCN systems were based on four-armed star diblock copolymers covering the composition range from $\varphi_A = 0.05$ to 0.50, end-linked via tetra-functional cross-links. The corresponding (uncross-linked) bulk melts of linear diblock and four-armed star diblock systems were also simulated using a recent DPD reparametrization (the same reparametrization was also the one employed for the conetworks) for comparison of the morphology results with those for APCNs, and for validation of our DPD methodology by comparison with the results of the original reparametrization study on linear diblocks. Our simulations provided APCN morphologies similar to those exhibited by their linear and star diblock counterparts, differing mainly at the polymer composition of $\varphi_A = 0.35$ where the conetworks organized into perforated lamellae, while both the linears and stars self-assembled into gyroids. Expectedly, at that composition, the shape parameters (asphericity, prolateness, and acylindricity) displayed the largest differences between the conetworks, on the one hand, and the linears and stars, on the other. Interestingly, when the segregation strength was sufficiently lowered from $\chi N = 60$ and 80 down to 40, the APCN with composition $\varphi_A = 0.35$ self-assembled into a gyroid morphology, suggesting that this morphology is also accessible to the present materials. The prevalence of the gyroid or the perforated lamellar morphology in APCNs with $\varphi_A = 0.35$ is the result of a delicate balance of forces, where the competition between the minimization of the interfacial energy and the minimization of elastic energy, commonly known as "packing frustration", also plays a major role. Uniaxial tension eventually transformed all originally unstretched APCNs, both self-assembled ($\varphi_A = 0.15$ to 0.50) and those in the disordered state ($\varphi_A = 0.05$ and 0.10), into lamellae normal to the direction of extension, with the APCNs possessing compositions of $\varphi_A = 0.15$ and 0.20, acquiring four different morphologies during the elongation process. When the present model APCN systems of equimolar composition ($\varphi_A = 0.50$) are sufficiently randomized by cleaving a high enough percentage (50%) of cross-links and either (again randomly, but in a different random way from the initial random cleavage) reconnected (partially or totally) or not, uniaxial stretching led to the formation of tilted lamellae. This latter finding reconciles, to some extent, earlier, apparently contradicting, results from previous studies, some of which yielded normal lamellae and some other parallel. We expect that the results of the present simulations would facilitate the design and development of next-generation APCNs.
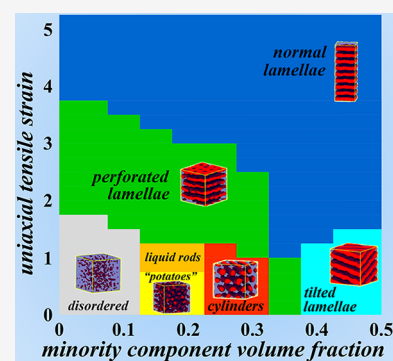
INTRODUCTION

First synthesized 35 years ago by two teams working independently on either side of the Atlantic Ocean,[1,2] amphiphilic polymer conetworks (APCNs) comprise cross-linked hydrophilic and hydrophobic polymer segments.[3] Thus, these relatively new soft materials represent an amalgamation of hydrogels and surfactants, combining a swellable elastic structure self-assembling both in water and in the bulk.[4] While possessing several emerging applications both in technology (matrices for solid/gel polymer electrolytes,[5−7] porous supports for phase-transfer enzymatic catalysis,[8] antifouling coatings,[9] and sequestering oil pollutants[10]), and in biomedicine (scaffolds for drug or nutrient delivery,[11] and tissue engineering, immunoisolation membranes serving as bioartificial

pancreas[12]), APCNs have a single high-added value application representing a global market of 10 billion US dollars annually: that of silicone hydrogel ("extended-wear") soft contact lenses.[13] In addition to vision correction, these APCN-based soft contact lenses may also be used for the delivery of ocular drugs, mainly ophthalmic antibiotics.[14] Two further exciting extensions of the use of the particular contact lenses currently
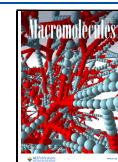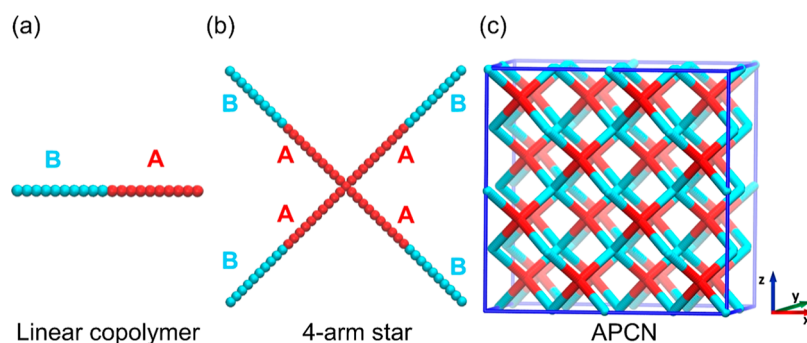
Figure 1. Schematic representations of the three polymer architectures whose self-organization in the bulk was modeled in this study using DPD: (a) linear diblock, (b) four-armed star diblock, and (c) APCN, all with 20-mer constituting chains/arms, with the examples depicted in the figure possessing an equimolar composition.

under development, both requiring the implantation of the appropriate microelectronics, are their application for glucose sensing for diabetics and serving as electronic television or computer screens.[15]

Being their most important physicochemical property, APCN self-organization has attracted much attention. However, the presence of the cross-links or/and the nonideal structure of the APCN building blocks lead to the formation of frustrated/distorted morphologies, with much less regularity than the morphologies observed with (non-cross-linked) linear block copolymers.[16] Thus, the APCN electron micrographs or atomic force micrographs usually exhibit morphologies with spheroidal domains, and the corresponding small-angle X-ray scattering (SAXS) or small-angle neutron scattering (SANS) profiles present a single broad peak.[5−7,10,17−38] However, recent synthetic developments, involving sparser and more regular cross-linking, e.g., end-linking, as well as the utilization of near-ideal building blocks (well-defined linear or star polymers), resulted in APCN nanophase-separated morphologies of high regularity, e.g., wavy lamellae,[39] and SAXS and SANS profiles with a number of higher order peaks.[39,40] The experimental recording of these more regular morphologies in self-assembled APCNs renders their modeling/simulation more worthwhile. In particular, current state-of-the-art simulations and self-consistent field theories (SCFT) very successfully reproduce the experimentally observed morphologies of linear diblock melts[41] and are, consequently, expected to accurately predict the morphologies formed by APCNs comprising well-defined building blocks.[42] Furthermore, any new morphologies, special to well-defined APCNs, and due to the presence of the cross-links, i.e., not exhibited by non-cross-linked systems, e.g., linear and star blocks, may first be identified by experiments and then confirmed by simulation/theory, or vice versa.

Our team were the first to pursue the modeling of APCN self-assembly in water or in the bulk.[43−46] Our approach involved the utilization of simple analytical expressions for the changes in the Gibbs free energy components (elastic, mixing, ionic, and interfacial) between the disordered and ordered states. While not state-of-the-art, our approach still provided useful results, yielding phase diagrams with the anticipated order of morphologies, i.e., disordered system, spheres, cylinders, and lamellae, as the volume fraction of the hydrophobic component increased and as the degree of ionization of the hydrophilic component decreased. State-of-the-art approaches on APCN modeling are scarce, and such recent examples include simulations by Wang and Müller[47]

and SCFT by Schmid and co-workers.[48] Both of these works considered APCN melts in two dimensions[49] and observed that the disorder−order transition occurred at a lower incompatibility when APCN thin films were subjected to elongation.

In the present work, we employ a state-of-the-art coarse-grained molecular dynamics simulations method, dissipative particle dynamics (DPD),[50−53] using the LAMMPS simulations engine[54,55] to simulate three-dimensional, rather than two-dimensional, APCN bulk melts (no solvent and no charge present in the system). Coarse-grained molecular dynamics simulations are useful in revealing the mechanical properties of polymers with complex structures, such as semicrystalline polymers,[56−62] double-network gels,[63−65] and block copolymers.[66−69] On the other hand, DPD simulations are effective in unveiling the self-assembly[70−72] and phase separation[73] processes in amphiphilic polymers. Thus, our simulation results will include both the morphological and mechanical properties of APCNs. The present APCN system comprised four-armed star diblock copolymers with 20-mer arms, end-linked via tetrafunctional linkers. Alternatively, the system may also be viewed as being composed of linear diblock copolymer 20-mers, cross-linked at each end via tetrafunctional linkers. Rather than just focusing on an equimolar system, our simulations covered the whole composition spectrum, with the minority polymeric component (block) spanning the whole range of volume fractions, from 0.05 to 0.50; because the system is symmetrical, there was no need to cover the other half of the polymer volume fraction range. The initial configuration of the system was a disordered one on a diamond lattice. In addition to the APCN melts, two other architectures were also simulated, linear diblock and four-armed star diblock bulk melts, with the same arm lengths and spanning the same composition ranges as the APCNs. Schematic representations of the equimolar linear diblock, equimolar four-armed star diblock, and equimolar APCNs are illustrated in Figure 1. In fact, we used the simulations of the linear diblock bulk melts to validate our method, according to the recent reparametrization by Huang and Alexander-Katz, which perfectly reproduced the phase diagram of linear diblock bulk melts.[74] This parametrization employed a density, ρ, of 5. Our simulation cells contained about 168 thousand beads, while an incompatibility χN value of 80 was employed in (most of) the simulations.[74]

■ SIMULATIONS METHOD

In DPD, the simulated particles obey Newton's equations of motion.[51] The total force acting on a certain particle arises

from its interaction with all its neighboring particles, located at a certain cutoff distance from it. This total force has four components: a soft bond force, a conservative (repulsive) force, a dissipative force, and a random force. It is common in DPD simulations to work in reduced units; thus, the thermal energy k_BT, the particle mass, and the cutoff distance are set equal to unity.

Any two successive particles in a polymer segment are connected via a soft harmonic bond with a spring constant K set here equal to its reparametrized value of 50.[74] The conservative (repulsive) force between any two particles decreases with their distance, ultimately vanishing at a certain distance. The maximum repulsion between two like particles, α_{ii}, is related to the density, ρ, and the thermal energy k_BT via[51]

$$\alpha_{ii}\rho = 75k_BT \tag{1}$$

with a reparametrized value of ρ of 5,[74] and the value of the thermal energy set equal to unity, eq 1 above gives

$$\alpha_{ii}=15 \tag{2}$$

The repulsion parameter for unlike particles, α_{ij}, can be calculated using the chosen value of the Flory−Huggins interaction parameter for unlike particles, χ_{ij}, from the following expression[74]

$$\alpha_{ij} \approx \alpha_{ii}+1.45\chi_{ij} \tag{3}$$

The random force captures the thermal fluctuations in the system. This force is directly proportional to the noise strength and inversely proportional to the square root of the integration time-step, δt, assigned here their reparametrized values of 0.10 and 0.015,[74] respectively.

The systems studied were described in the Introduction section and illustrated schematically in Figure 1. The inner segments of the stars comprise type A beads colored red. The initial (and "maximally swollen") network conformation would be that of a diamond lattice, as shown in Figure 1c. To explore the effect of polymer composition on the self-assembly in all three polymer architectures, the number of type A beads was varied from 1 to 10, corresponding to A volume fractions φ_A = 0.05−0.50, varying at 0.05 increments. For example, a star with φ_A = 0.10 consists of 2 beads of type A and 18 beads of type B, the former being connected with the star's core. Systems with φ_A values greater than 0.50 were not examined since, by construction, APCNs are symmetric, i.e., the φ_A = 0.30 system yields identical results to that with φ_A = 0.70.

Cubic simulation cells were constructed for all three polymer architectures, setting the density, ρ, equal to 5, and imposing periodic boundary conditions in all three directions. The APCNs were generated by replicating a perfect diamond lattice initial configuration to construct the cubic cell. Figure 1c depicts a $4 \times 2 \times 4$ network formed by replicating a diamond lattice configuration four times in the x-direction, twice in the y-direction, and four times in the z-direction. Simulations for the APCNs were executed using $12 \times 6 \times 12$ systems comprising ∼71,000 beads. To ensure that the outcomes of the DPD simulations did not suffer from system-size effects, all runs were repeated using $16 \times 8 \times 16$ networks of ∼168,000 beads. The accumulated simulation results of the larger cells verified the microstructures obtained with the smaller cells, thereby confirming the absence of system-size effects. Unless otherwise stated, the APCN results presented in this paper originated from the $16 \times 8 \times 16$ networks. As already mentioned, DPD simulations of linear and star copolymers

were also conducted. More details regarding the composition and size of all simulated systems are provided in Table 1. All

Table 1. Number of Molecules, Number of Particles per Molecule, Length of Simulation Box, and Volume Fraction Range in A Component, φ_A, Employed for the Present Simulations on the Three Model Systems of Different Architecture Studied in this Work

system architecture	number of molecules	number of particles per molecule	length of simulations box	φ_A
linear	6750	20	30	0.05−0.50
star	1667	81	30	0.05−0.50
APCN	1	167,936	32.26	0.05−0.50

runs were carried out using the LAMMPS simulations engine.[54,55] Huang and Alexander-Katz[74] showed that for Flory−Huggins incompatibility parameter values, χN, in the range 80−95, linear diblocks exhibit a rich-phase behavior assuming spherical, cylindrical, gyroid, and lamellar microstructures, as a diblock composition is varied. Thus, throughout most of this work, the repulsion parameter between beads of types A and B, α_{ij}, was set equal to 20.8, corresponding to a Flory−Huggins incompatibility parameter value, χN, equal to 80.

To prepare the randomly mixed state for the initial condition, the simulation is performed by setting the interaction potential α_{ij} equal to $\alpha_{ij} = \alpha_{ii} = 15$ (i.e., deactivating the incompatibility between the two bead types) for time $t = 15 \times 10^3\tau$. The same protocol was also applied to the linear and (free) star copolymers. Subsequently, the interaction potential value was increased to $\alpha_{ij} = 20.8$, and the amorphous APCN configurations were subjected to equilibration for at least $t = 4.5 \times 10^5\tau$. On the other hand, due to the absence of cross-links and, consequently, their enhanced ability to rearrange compared to that of the APCNs, linear and star bulk systems assumed their equilibrium microstructures much faster, within less than 10^7 DPD steps corresponding to $t = 1.5 \times 10^5\tau$.

Selected equilibrated APCN microstructures from all volume fractions were subjected to tensile deformation simulations, and the following procedure was employed to investigate their mechanical response. The equilibrated cubic simulations cells were stretched in the selected direction, e.g., the x-direction, at a constant engineering strain rate given as $\dot{\varepsilon} = [L_x(t) - L_x(t = 0)]/L_x(t = 0) = 1.25\times10^{-5}$, where L_x denotes the length of the orthogonal cell in the x-direction. At the same time, the box lengths in the other two directions, i.e., y- and z-directions, were decreased to keep the box volume constant. This implies that the Poisson's ratio, μ, is equal to $\mu = 0.5$. Then, the stress σ in the x-direction is calculated as $\sigma = -P_{xx} + (P_{yy} + P_{zz})/2$, with P_{xx}, P_{yy}, and P_{zz} being the components of the pressure tensor. Tensile deformation simulations were carried out for at least 20×10^6 DPD steps to obtain engineering strain ε values greater than $\varepsilon = 3$.

■ RESULTS AND DISCUSSION

Morphologies. Figure 2 depicts the morphologies obtained from our simulations for all three architectures, conetworks, four-armed stars, and linears, all comprising 20-mer diblocks, with the conetworks composed of four-armed star diblocks end-linked by tetra-functional linkers, as a
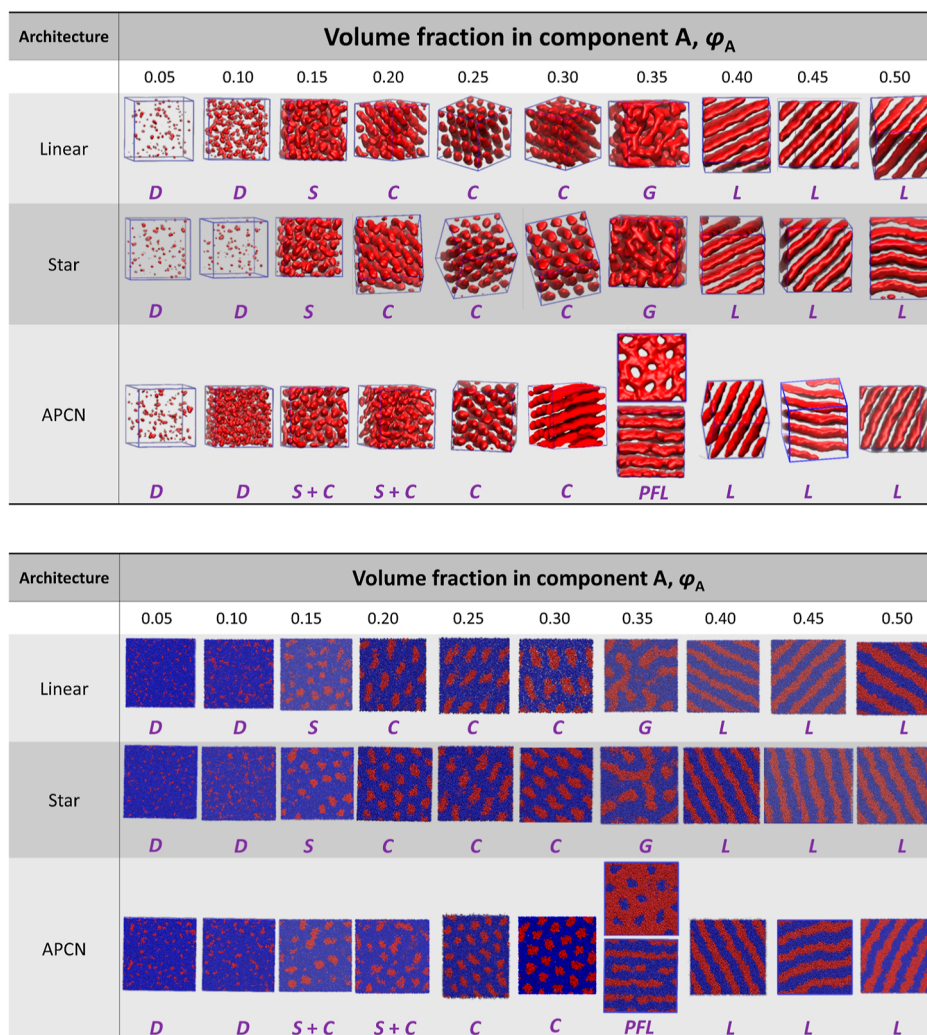
Figure 2. Morphologies obtained for all three architectures, as a function of the minority component polymer volume fraction, φ_A, illustrated as three-dimensional representations (top) and cross-sections (bottom). In the top part of the figure, only the minority component is shown (in red) for clarity (majority component is omitted), whereas, in the bottom part of the figure, the cross sections of the cylinders in the C (at $\varphi_A = 0.25$) and PFL (at $\varphi_A = 0.35$) microphases were sampled not vertically to the cylinder axis but at an angle so as to clearly differentiate their projection from that of spheres. Key: D: disordered, S: spheres, C: cylinders, PFL: perforated lamellae, G: gyroids, and L: lamellae.

function of the minority component polymer volume fraction, φ_A, spanning the range from 0.05 to 0.50. In the figure, the morphologies are displayed in two different ways: three-dimensional representations (top) and cross-sections (bottom).

By inspection of the above morphologies, the following conclusions may be drawn. First, the linear diblock bulk melts faithfully reproduced the morphology sequence (D → S → C → G → L) determined by Huang and Alexander-Katz using their reparametrized DPD simulation,[74] thereby validating our method. Moreover, our results on star diblock bulk melts exhibited morphologies identical to those of the linear diblocks. These star diblock bulk melt morphologies are in agreement with those from the SCFT by Matsen and Schick on similar star diblock bulk melts.[75] Our results on the morphologies of the star diblock bulk melts are also very similar, but not identical, to the those from the DPD simulations on star diblock bulk melts by Xu et al.,[76] which gave a G, rather than a C, morphology at $\varphi_A = 0.30$. Furthermore, our simulated morphologies for the conetwork bulk melts were similar, but not identical, to our simulated

morphologies for the linear and star diblock bulk melts, slightly differing in two minority component polymer volume fraction ranges, φ_A; first, at $\varphi_A = 0.35$ where the conetworks missed G and presented, instead, PFL, and, second, at $\varphi_A = 0.15$ and 0.20, where conetworks presented mixtures of S + C ("potatoes") rather than individual/clear S or C.

Thus, the presence of the end-linking in the APCNs leads to the above-mentioned morphology differences compared to their linear and star counterparts at the corresponding φ_A-values and the same segregation strength. The appearance of PFLs in conetworks at a φ_A-value of 0.35 deserves special attention. The PFL morphology is not observed in star diblocks (both in the present results and those from SCFT[75]) at the present segregation strength of $\chi N = 80$. However, it has been observed at lower segregation strengths, $\chi N = 20$ and 30, both with four-armed star diblocks and four-armed miktoarm stars (comprising two different types of homopolymer arms, two from each type).[76] Interestingly, the PFL morphology has been identified both in AB$_2$ three-armed miktoarm stars and comb copolymers at the same segregation strength as in this study, $(\chi N)_{effective} = 30$,[77] and at a nearby φ_A-value of 0.30, and
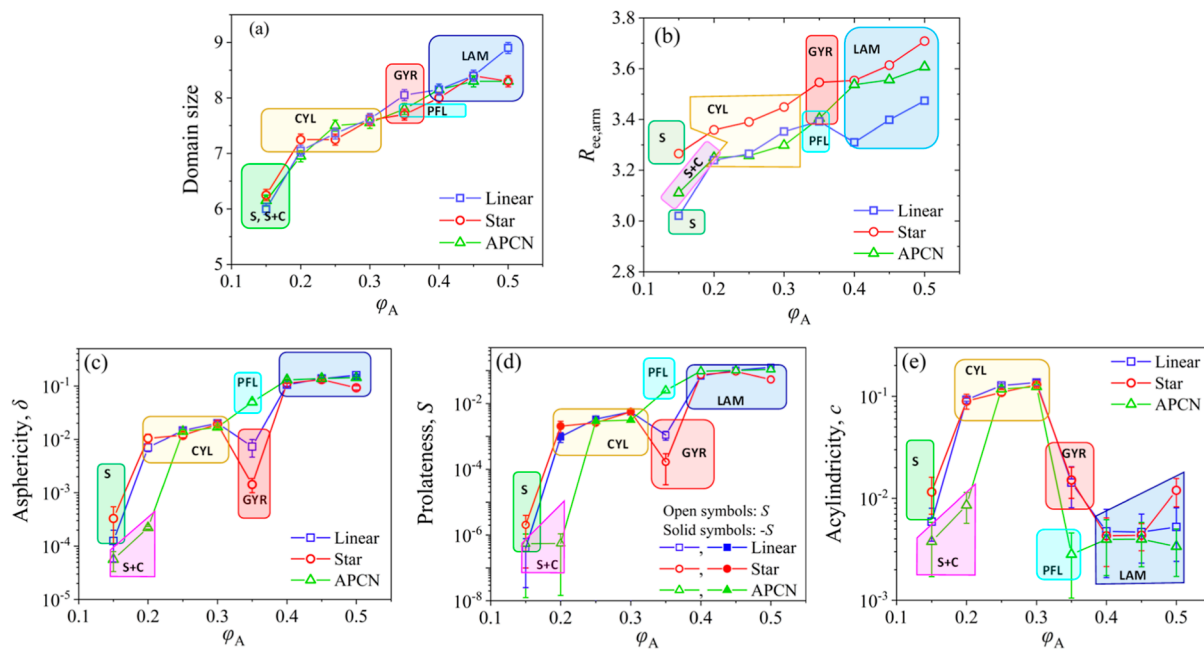
Figure 3. Composition dependence of the (a) domain size, (b) diblock chain end-to-end distance, and (c−e) shape parameters for the morphologies assumed by the three architectures studied, APCNs, stars, and linears.

it has also been predicted to appear in diblock-homopolymer (majority component) blend melts.[77] For this last case, the stabilization and prevalence of the PFL morphology has been explained by the reduction in packing frustration (competition between minimization of interfacial energy and minimization of elastic energy) that results from the extra thickness of the majority-component layers, and a similar explanation may be given for miktoarm stars, combs,[77] and, presumably, conetworks as well. Importantly, the PFL morphology has very recently been identified, both experimentally and via DPD simulations, as a stable (equilibrium) bulk morphology in a particular type of highly branched and segmented comb architecture, that of diblock Janus-type "A-branch-B" bottle-brush copolymers (di-JBBCP) at $\varphi_A = 0.34$.[78] Although not with a network architecture, di-JBBCPs are highly branched, similar to APCNs.

Regarding the speed of attainment of the final equilibrium morphology, we stress that this was much slower for the conetworks than for the linears and stars, especially for the φ_A-value range from 0.35 to 0.50. Sometimes, the APCNs would get stuck to a metastable doubly connected lamellar structure. To facilitate equilibration, we would anneal the system to dimensionless temperatures, T, of up to 1.2 and then quench back down to $T = 1$.

Confirmation of Morphology Equilibration. To further support our claim that the above-determined morphologies are the equilibrium ones, we repeated some of the simulations at ($\varphi_A = 0.35$) or near ($\varphi_A = 0.25$ and 0.40) the critical composition range by changing two important parameters. One was the system configuration at the start of the simulation and the other was the system size. Regarding the former, we started the simulation with the system not at the disordered state, but at a nearby (with respect to the conetwork composition) equilibrium morphology, and changed the composition to the desired one just before the beginning of the simulation. We did this for five cases, in all five of which the simulations again yielded the same structures as those

obtained when starting from the disordered state. These results are given and discussed in the Supporting Information, where relevant figures (Figures S1−S4) and videos (Videos S1, S2, S3 and S4) are also provided. Regarding the latter, we studied again the APCN with $\varphi_A = 0.35$, also starting the simulation from the disordered state, but employing system sizes twice as large (328,000 beads) and half (70,848 beads) of our standard (full) size system (167,936 beads). For both of these additional simulations, the PFL morphology was again obtained, with the results being presented and discussed in the Supporting Information (Figure S5).

Domain Size, Chain End-To-End Distance, and Shape Parameters. To more quantitatively analyze the equilibrium morphology structures depicted in Figure 2, we calculated from them the various size parameters, including the domain sizes, the linear chain end-to-end distances, and the shape parameters, all plotted against the minority component polymer volume fraction in Figure 3. The end-to-end distances were calculated for the linear constituting segments, i.e., the diblock copolymer chain ("arm"), $R_{ee,arm}$, to enable a fairer comparison among the three polymer architectures. Thus, these distances concerned the diblock chain for the linear system, a diblock arm for the star block system (rather than the whole star), and the linear diblock chain between two consecutive cross-linking points for the conetwork system. On the other hand, the domain sizes were calculated as the distance of the second peak in the radial pair correlation function of the minority component. Finally, the shape parameters, i.e., asphericity, prolateness, and acylindricity,[79,80] were calculated from the three invariants, I_1, I_2, and I_3, which are correlated to the three eigenvalues of the gyration tensor, λ_1, λ_2, and λ_3, as shown in Appendix S1 in the Supporting Information.

Figure 3 shows that for all three architectures both the domain size and the linear diblock chain end-to-end distance expectedly increase as the minority component polymer volume fraction increases. Moreover, for a given composition,

the differences in domain size and linear diblock chain end-to-end distance are small among the three architectures, even when there is a morphology difference (note that the prevailing morphology is also indicated in the five plots in the figure) between the conetworks and the two other architectures, e.g., at $\varphi_A = 0.35$. Furthermore, there is a rather clear trend in the diblock chain end-to-end distance, where this distance for the stars and the APCNs is systematically greater than that for the linears. This can be attributed to the fact that the arms in the two branched architectures, stars and APCNs, are more stretched as compared to the linears whose two chain ends are both free.[81]

Turning now our attention to the three shape parameters, asphericity, prolateness, and acylindricity,[79,80] it seems that, in contrast to the domain size and diblock chain (arm) end-to-end distance, at the minority component polymer volume fraction where the conetwork architecture gives a different morphology from the linear and star counterparts, the shape parameters become greatly differentiated. This is the case at φ_A-values of 0.20 and 0.35, where the conetwork architecture forms S + C and PFL, respectively, while the two other architectures, respectively, form C and G at the same φ_A-values. This differentiation in the values of the shape parameters when the morphologies become architecture dependent is because the shape parameters are highly shape sensitive. Thus, the morphologies in the three diblock copolymer systems of different architectures, conetworks, stars, and linears, could also be successfully identified from their asphericity, acylindricity, and prolateness values, quantitatively.

We now examine separately the trends in the three shape parameters. First, concerning asphericity, as φ_A increases, with the exception of linears and stars at $\varphi_A = 0.35$, asphericity increases too, denoting the transition from the S morphology at low φ_A values all the way to the L morphology at higher φ_A values, via the S + C, C, PFL, and G morphologies. The APCN asphericity at a φ_A-value of 0.2 is lower than that for linears and stars as the latter two architectures have transitioned to C, whereas conetworks still form S + C. At φ_A values of 0.25 and 0.30 all architectures exhibit the same asphericity values, as all three also organize to the same morphology, C. Asphericities also become approximately equal for the three architectures within the φ_A value range from 0.40 to 0.50, where they all self-assemble to L. The discrepancy observed in asphericity for a φ_A value equal to 0.35 is due to the morphology difference, with the linears and stars acquiring the G structure where the constituting chains have a more spherical conformation than in the PFL structures formed by the conetworks.

Similar observations and explanations may be given regarding the plot with the prolateness. First, at low φ_A values where the S morphology prevails, prolateness is low. At higher φ_A values, when the C morphology is attained by the three architectures, the chains constituting the cylinders acquire an oblate, rather than a prolate conformation, i.e., they exhibit slightly negative prolateness values (note the sign reversal in the plot, so as to preserve positive values for the logarithmic y-axis). For the highest φ_A values, where L are formed, prolateness values are the highest too, as the constituting block copolymer chains adopt an elongated conformation to be efficiently packed in this lowest curvature morphology. Finally, regarding the acylindricity plot, the lowest acylindricity values are expectedly exhibited for L due to the rather cylindrical (and prolate) chain conformation of the constituting chains packed

in this morphology, and for the S and S + C morphologies as perfect spheres also exhibit vanishing acylindricity. The acylindricity for the C morphology is the highest because the constituting chains acquire the oblate conformation to pack most efficiently, as already mentioned in the discussion of the prolateness. Note that acylindricity (as well as prolateness and asphericity) does not refer to the morphology as a whole, e.g., cylindrical, but to the individual diblock copolymer chains making up the various morphologies. For the cylindrical morphology, the constituent diblock copolymer chains are in a disklike and, consequently, oblate, nonprolate, and, therefore, acylindrical conformation. This can explain the apparent paradox that the cylindrical morphology exhibits the highest acylindricity.

Thus, our results on the morphologies and size parameters of the conetwork melts presented above are similar, but not identical, to those of the corresponding linear diblock copolymer and star diblock copolymer systems also investigated in the present work. The three plots in the lower part of Figure 3 clearly demonstrate the polymer compositions for which APCNs self-organize into a different structure as compared to their linear and star counterparts. It is also noteworthy that the evolution of the conetworks to their equilibrium morphology was slower than those for linears and stars by a factor of 3−4.

Effects of Segregation Strength, Cross-Link Removal, and Chain Length on Morphologies. Before proceeding to the study of their tensile mechanical properties, we briefly examined if the morphologies of the conetworks at ($\varphi_A = 0.35$) or near ($\varphi_A = 0.40$) the critical composition range are affected by the segregation strength (χN values) and the elastic chain length, N. Thus, we first changed the χN incompatibility parameter from the initial value of 80 to three other values, 40, 60, and 110. We observed that, while at the two higher χN values of 60 and 110, the morphology reached at equilibrium was still the PFL one, the same as that at a χN value of 80, the morphology reached at the lowest χN value of 40 was very interestingly the G one! Thus, APCNs can also access the G morphology, provided that the segregation strength is sufficiently lowered. Similar to APCNs, three-armed AB_2-type miktoarm stars (at $\varphi_A = 0.30$) also equilibrate into Gs and PFLs at lower and higher segregation strengths, respectively.[77] The results of these simulations are given and discussed in the Supporting Information (Figure S6). The fact that the G morphology is attained by the APCNs at a segregation strength lower than that of the linear diblock and four-armed star diblock counterparts might have to do with the fact that the degree of polymerization in APCNs is not N (=20, in the case of linears and the arms of the present stars) but infinite, owing to the interconnectivity of the APCN components into a gigantic molecule, leading to a larger effective χN value.

To support the above hypothesis of APCN infinite size, we performed simulations at the standard χN value of 80 but after randomly removing tetrafunctional linkages among the four-armed star diblocks constituting the APCNs at $\varphi_A = 0.35$. Tetrafunctional linkages were randomly removed at four different percentages, 25, 50, 75, and 95%. Whereas equilibration of the APCNs with their linkages removed at the three lower percentages gave again PFLs, the APCN with its linkages removed at a percentage of 95% yielded G, thereby (indirectly, at least) supporting the infinite molecular weight hypothesis for pristine APCNs. These results are again

provided and discussed in the Supporting Information (Figure S7).

Regarding the effect of the elastic chain length, N, in the conetworks, we examined APCNs with $\varphi_A = 0.40$ and $\chi N = 80$, and at one N value lower and the other higher than the standard value employed in the rest of this study of $N = 20$. Thus, APCNs with N values of 10 and 30 were explored. Upon equilibration, these two APCN systems also yielded Ls, the same morphology as that exhibited by our standard APCN system with $N = 20$ (and the same χN and φ_A values). These results are illustrated and discussed in the Supporting Information (Figure S8).

Stress-Strain Curves. We now turn our attention to the response of conetwork bulk melts to uniaxial tension. Figure 4
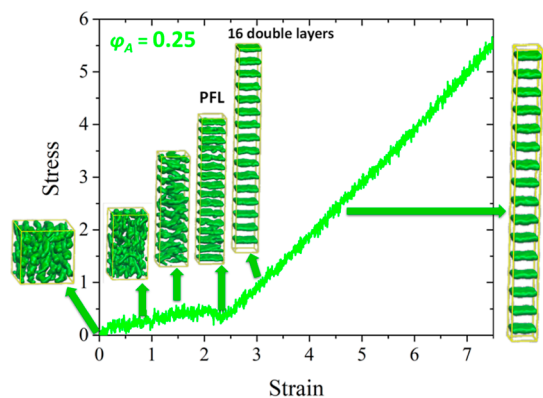
Figure 4. Tensile stress–strain curve for APCN with $\varphi_A = 0.25$ and $\chi N = 80$. Snapshots during the elongation are also shown, indicating the transformation of the initial cylindrical morphology into perforated lamellae and lamellae normal to the direction of tension.

plots the stress response of the conetwork bulk melt with a polymer volume fraction of the minority component, φ_A, of 0.25, to uniaxial tension. At this composition, the system is organized into the C morphology (see also Figure 2). The axes in the figure are tensile stress and tensile strain. One can see from Figure 4 that, at relatively small elongations, up to a tensile strain of about 2.5, the system responds to the extension as a soft material, but, at elongations higher than 2.5, the system hardens, displaying a much greater slope in the stress–strain curve. This strain-hardening behavior can be attributed to the fact that the constituting polymer chains have unfolded to a great extent, and also the cross-linking points have segregated into layers which include only adjacent cross-linking points.[66−69] At this critical tensile strain, the system has almost attained the morphology of "normal lamellae." It must be pointed out that the present system with a φ_A value of 0.25 has already transformed gradually from the initial (absence of deformation) C morphology into PFLs at a strain of 1.25, before its final transformation into normal lamellae at a strain of 2.75. Snapshots with the aforementioned morphologies are also depicted in Figure 4.

In this paragraph, we compare the results presented in Figure 4 above with those of a rare study by Mortensen and Annaka,[82] involving an APCN with a minority polymer volume fraction of about 0.30, but also containing a selective solvent, and, in particular, 70% of water (and 30% of pure APCN). When unstretched, this system is organized into cylinders (C). However, upon subjecting the system to a strain of about 2, the cylinders become oriented perpendicular to the direction of

strain. At the same time, a lamellar structure, also perpendicular to the applied strain, appeared too (although possible water evaporation may have been important for the appearance of the lamellae), coexisting with but being more intense than the cylindrical structure. Thus, this experimental study corroborates our simulation results, in suggesting that a strain of at least 2 is necessary to achieve orientation of the microphases, which may also include lamellae perpendicular to the direction of strain.

The APCNs of all compositions were subjected to uniaxial tension, and the results are presented in Figure 5. All tensile stress–strain curves in Figure 5 are qualitatively similar to that in Figure 4, with a strain-hardening behavior appearing at a strain also around 2.5. Importantly, the two conetworks with very small polymer volume fractions of the minority component, $\varphi_A = 0.05$ and 010, being in the disordered state when unstretched, organize into PFLs and then to normal lamellae when subjected to strains of 1.75 and 3.75, respectively. Moreover, all APCNs give normal lamellae when stretched at or beyond the point of strain hardening. Finally, APCNs with φ_A-values of 0.15 and 0.20 seem to exhibit four different morphologies during the course of their elongation.

Direction, Repeatability, and Relaxation of Deformations. The deformations were applied in all three directions, and it was determined that they had only a small effect on the stress–strain curves (small differences observed only for smaller strains lower than 4). Such an example is provided and discussed in the Supporting Information (Figure S9). The repeatability of the deformations was also examined by starting the simulations from a number of different, independent (equilibrated) configurations. Only small changes were observed again, with those small differences taking place within the strain range between 0.8 and 4. An example for this is given and discussed in the Supporting Information (Figure S10). Finally, it was examined if the configurations observed during deformation are at equilibrium or if they would relax into a different conformation when sufficient time is provided to the system. For this, we chose several values of strain on a stress–strain curve and allowed the stress at each point to relax under constant strain. We found that all stresses, corresponding to strains higher than 1, had already relaxed; only the stress corresponding to a strain value equal to 1 had not fully relaxed. The results for this investigation are given and discussed in the Supporting Information (Figures S11−S15, and Videos S5 and S6).

Strain-Composition Morphology Phase Diagram. The points of morphological transitions in Figures 4 and 5 are summarized in Figure 6 in the form of a morphology phase diagram with axes strain, ε, and minority component polymer volume fraction, φ_A. First of all, the diagram clearly shows that when sufficient elongation is applied, all APCNs organize into normal lamellae. This is due to the high regularity of the conetworks, including the absence of entanglements (diamond lattice), allowing the segregation of the two types of segments (and the cross-links) into their respective layers upon the application of a sufficiently high tensile strain.[66−69] Attainment of normal lamellae is most easily (at the lowest strain) observed at a φ_A-value of 0.35, at which composition the unstretched APCN already organizes into PFLs. It is interesting to note that at φ_A-values of 0.30 or lower, the conetworks acquire the PFL morphology before transforming into normal lamellae. In contrast, at φ_A-values of 0.40 and
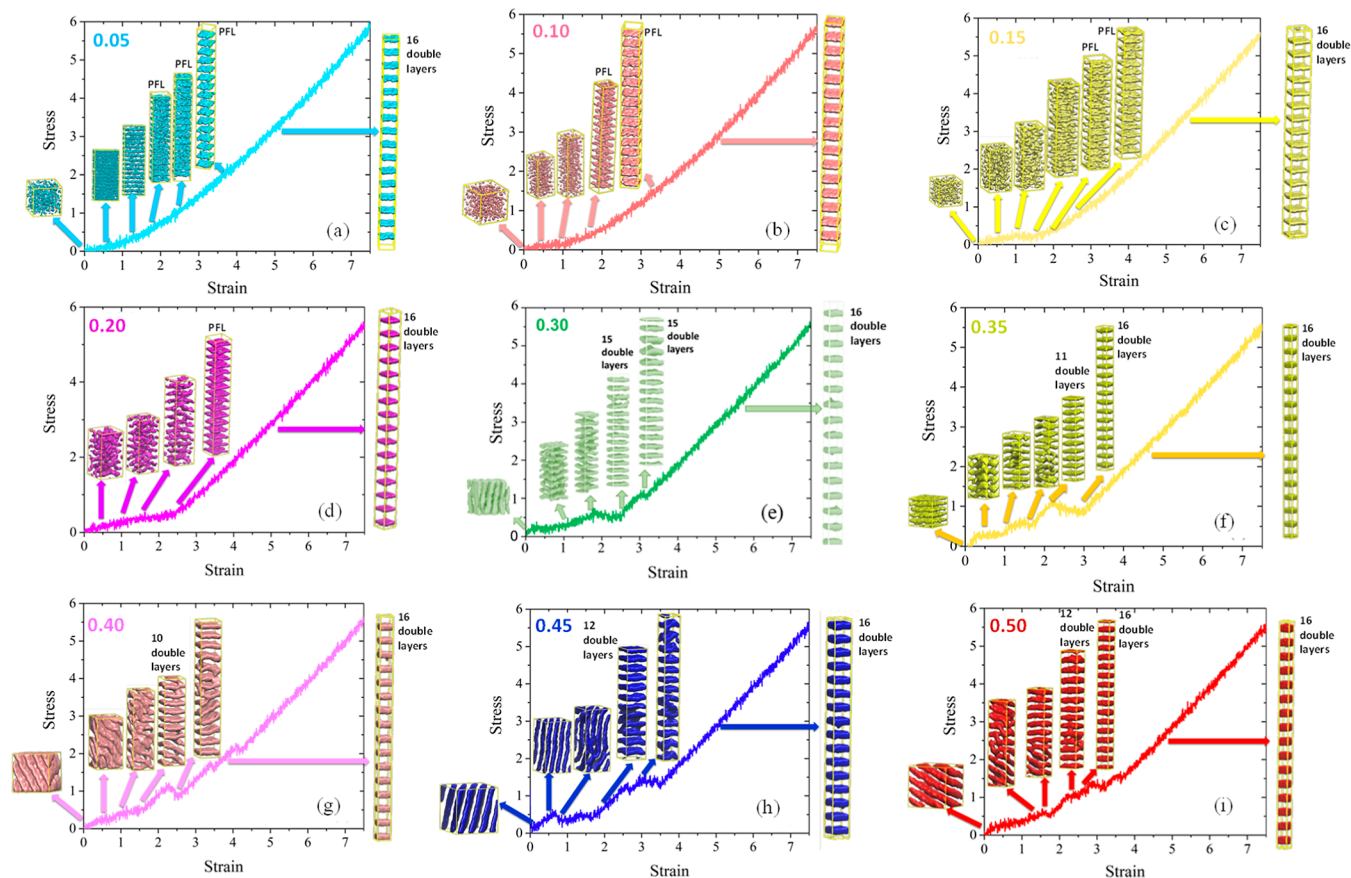
Figure 5. Tensile stress−strain curves for the conetworks with φ_A in the range from 0.05 to 0.50, except for the sample with $\varphi_A = 0.25$, whose stress−strain curve (and relevant snapshots) is already presented in Figure 4. The evolution of the morphology during elongation is also illustrated via relevant snapshots.
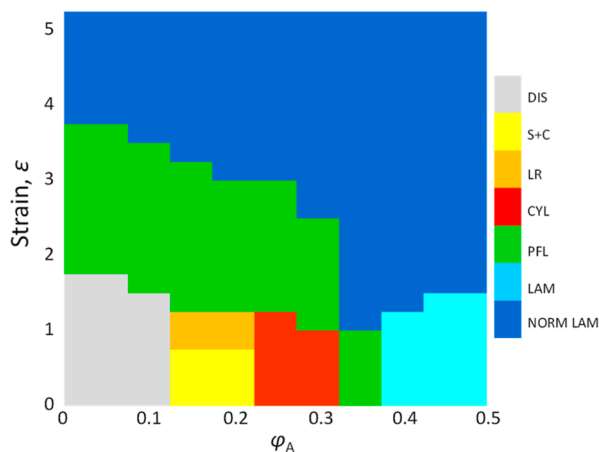

Figure 6. APCN morphology phase diagram with respect to tensile strain, ε, and minority polymeric component volume fraction φ_A.

higher, the unstretched conetworks form tilted lamellae, transforming into normal lamellae when subjected to strains of 1.25−1.50. However, the richest phase behavior is observed in the former φ_A-value regime, with the appearance of three different morphologies (including the disordered one) when $\varphi_A = 0.05-0.10$ and 0.25−0.30, and the appearance of a record of four different morphologies when $\varphi_A = 0.15-0.20$.

The previously identified morphology reorientation from tilted to vertical lamellae relative to the applied force is very important. This reorientation is likely to greatly affect the

macroscopic properties of the material. The transport properties (e.g., diffusion) can be such an example, arising from the fact that one phase may be transporting[83]/conductive[84] but the other barrier/insulating. Thus, the material can be transformed from an insulator into a conductor, or vice versa, simply by applying a tensile force. This implies that the material can be used as an on−off switch with applications in electronics. The more complex APCN behavior, not previously observed, with multiple transitions, e.g., for APCNs with $\varphi_A = 0.15-0.20$, may further enrich the application possibilities of the present materials, facilitating the development of adjustable switches.

Orientation of Lamellae upon Stretching. Our result, on the lamellae acquiring an orientation normal to the direction of the elongation, concerns our APCN system which is model and is in agreement with the results of Escobedo[66−69] and Schmid[85] on similar model APCN systems in the bulk. When the APCN system is not model but randomly cross-linked, there is both theoretical[86] and experimental[87] evidence suggesting that stretching directs the lamellae into an orientation parallel, rather than normal, to the elongation axis. To investigate this latter result using our present tools, we transformed our equimolar APCN system ($\varphi_A = 0.50$) into a less perfect one by introducing some randomness in the cross-links. We did that using two different approaches: in the first one, we randomly cut some of the cross-linking points in the initially disordered system, allowed the system to equilibrate, and then stretched it; and in the second approach, we again randomly cut some cross-links, then randomly reconnected (in a different random way) some or all
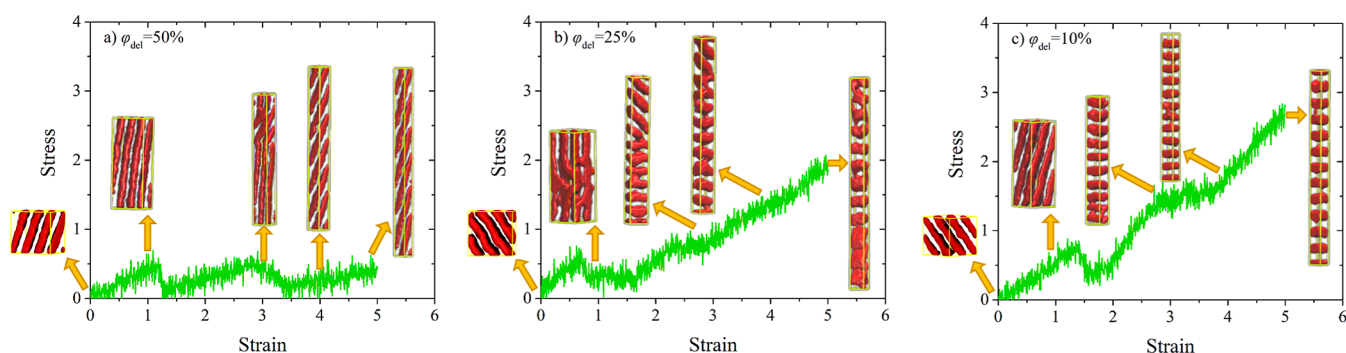
Figure 7. Tensile stress−strain curves for conetworks with $\varphi_A = 0.50$ and $\chi N = 80$, whose cross-links were first removed in a random fashion at percentages of (a) 50, (b) 25, and (c) 10%, equilibrated (all gave tilted lamellae) and subjected to uniaxial elongation. Relevant snapshots, illustrating the evolution of the lamellar orientation during elongation, are also depicted.
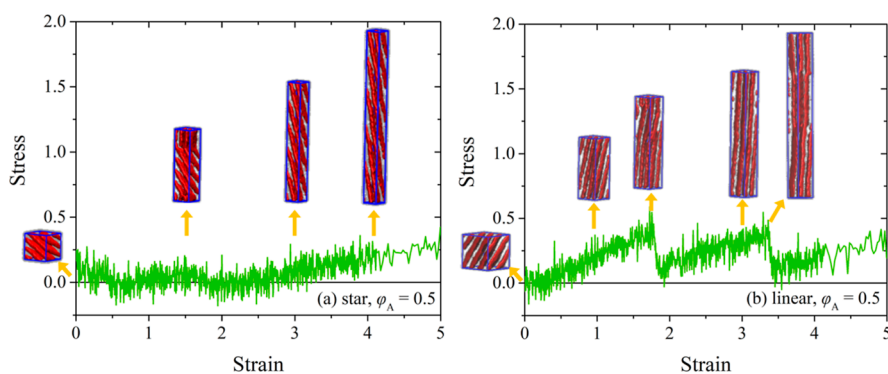

Figure 8. Tensile stress−strain curves and relevant snapshots for lamellae formed by (a) star and (b) linear bulk melts with $\varphi_A = 0.50$ and $\chi N = 80$.
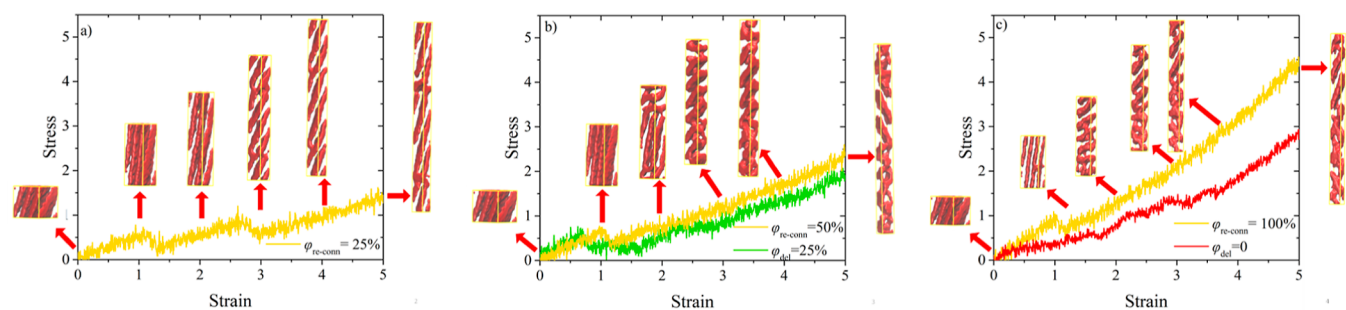

Figure 9. Tensile stress−strain curves for conetworks with $\varphi_A = 0.50$ and $\chi N = 80$, whose cross-links were first removed in a random fashion at percentages of 50% and then randomly reconnected at (a) 25% (leaving 37.5% deleted cross-links), (b) 50% (leaving 25% deleted cross-links), and (c) 100% (leaving 0% deleted cross-links), equilibrated (all gave tilted lamellae), and subjected to uniaxial elongation. Parts (b,c) of the figure are overlaid with similar APCN systems with the same overall cross-linker concentration. Relevant snapshots, illustrating the evolution of the lamellae orientation during elongation, are also depicted.

of the cross-links, and equilibrated the system and finally stretched it.

Figure 7 illustrates the results from the first cross-link randomization approach, where (a) 50, (b) 25, and (c) 10% of the cross-links were deleted in a random fashion in the initially disordered APCN system with $\varphi_A = 0.50$, which was then allowed to equilibrate and was finally subjected to elongation. After equilibration, all three systems were organized into tilted lamellae, which were subsequently subjected to uniaxial elongation. The resulting tensile stress−strain curves and selected snapshots are depicted in Figure 7.

The figure shows that the tilted lamellae formed in the two systems with the lowest percentage of randomly removed cross-links, 10 and 25%, were reoriented to normal lamellae upon elongation. This reorientation was completed at a lower

strain for the system with a lower percentage of cross-links removed, 10%. In contrast, for the system with the highest percentage of cross-links removed, 50%, the lamellae remained tilted, at least within the strain range investigated. Thus, although we did not reproduce in the present study the previous results from theory[86] and experiments[87] on the parallel orientation of the lamellae, we, nonetheless, showed that sufficient randomization of the system destroys the vertical orientation of the lamellae relative to the direction of strain, and the system ends up in a configuration of tilted lamellae.

Interestingly, lamellae formed by totally free (uncross-linked) star diblock bulk melts with $\varphi_A = 0.50$ also remain tilted upon uniaxial elongation, as shown in Figure 8a, as this latter system is approximately equivalent to the APCN system of the same φ_A value and half of its cross-links removed. In

contrast, upon uniaxial tension, the lamellae formed by the linear diblock bulk melts with $\varphi_A = 0.50$ also become highly aligned in the direction of the elongation, as illustrated in Figure 8b. Thus, almost complete orientation of the lamellae parallel to the direction of elongation is obtained when all cross-links and star cores (internal star cross-links) are removed.

The results from the second approach for cross-link randomization are depicted in Figure 9. As mentioned above, in this case, 50% of the APCN cross-links were first randomly removed, and then three different percentages of cross-links, (a) 25% (leaving 37.5% deleted cross-links), (b) 50% (leaving 25% deleted cross-links), and (c) 100% (leaving 0% deleted cross-links), were reinstalled also in a random way but not identical to that of their removal. The three APCN systems were afterward equilibrated and stretched. After equilibration, all three systems yielded tilted lamellae, which, upon elongation (stress−strain curves in dark yellow in Figure 9), remained tilted lamellae but at various angles, as illustrated in Figure 9. In parts (b and c) of the figure, the presently recorded stress−strain curves (in dark yellow) are compared to the previously presented stress−strain curves of similar systems with the same percentage of cross-links.

Regarding part (c) of Figure 9, the stress−strain curve of the APCN system having back 100% of its cross-links (but doubly randomized, shown in dark yellow) is overlaid with the stress−strain curve of the APCN system in Figure 5i having also 100% of the cross-links but in an orderly manner (shown in red). The former curve displays higher stress values over the whole range of strain values accessed. This can be attributed to the fact that the randomization of the cross-links in the former system also leads to chain entanglements, resulting in a higher effective cross-linking density and, ultimately, to a stronger stress response. One may recall from Figure 5i that the model APCN system acquired a normal lamellae morphology from a strain of just above 1.5, at which strain the corresponding randomized APCN system has a tilted lamellar morphology.

Finally, examining part (b) of Figure 9, the stress−strain curve of the APCN system having 75% of its cross-links (but doubly randomized, shown in dark yellow) is plotted together with the stress−strain curve of the APCN system in Figure 7b having also 75% of the cross-links but in a more orderly fashion than in the former system (shown in green). The former system exhibits (slightly) higher stresses for most of the strain range investigated, above strain values of 1, something again attributable to the presence of entanglements in the former system. Note that the more model APCN system depicted in Figure 7b started to revert to a normal lamellar morphology already from a strain of 3, whereas the doubly randomized APCN system keeps a totally tilted lamellar morphology up to a strain of 5.

CONCLUSIONS

We presented a thorough DPD simulation study on model APCN bulk melts comprising linear diblock copolymers end-linked by tetrafunctional cross-links, covering the whole composition range, to obtain their self-assembled morphologies and investigate their tensile behavior. For a large part of the composition space, these APCN bulk melts yield morphologies identical to those formed by (nonend-linked) linear and star bulk melts (also simulated in this investigation), with differences located at $\varphi_A = 0.15$ and 0.20 where the APCNs formed mixtures of spheres and cylinders rather than

pure spheres or cylinders, and at $\varphi_A = 0.35$ where the APCNs formed perforated lamellae rather than gyroids. These differences manifest a limited but potentially decisive effect of end-linking (with concomitant lack of free chain ends) on the self-assembled structures formed by the APCNs. Sufficient uniaxial elongation (strains > ∼1−4, depending on the APCN composition) of APCNs of all compositions ultimately resulted in morphology transformation into lamellae oriented normally to the elongation direction, with APCNs of intermediate composition, $\varphi_A = 0.15$ and 0.20, exhibiting a rich morphological behavior with respect to strain, and a record of four different morphologies. Partially impairing the model nature of APCNs at $\varphi_A = 0.50$, via the random cleavage of a sufficient percentage of cross-links (with or without their random, again, reformation), has an impact on the morphology obtained at high elongation, which is now tilted lamellae rather than normal. It is noteworthy that tilted lamellae are also formed by stretched equimolar ($\varphi_A = 0.50$) star diblock bulk melts but not by stretched equimolar linear diblock bulk melts which form parallel lamellae. Future work will involve extending our DPD simulations to APCN systems swollen in a selective solvent, e.g., water, and introducing (smeared) electrical charge into the hydrophilic segments.

ASSOCIATED CONTENT

ⓢ Supporting Information

The Supporting Information is available free of charge at https://pubs.acs.org/doi/10.1021/acs.macromol.3c01392.

> Definitions of the invariants and shape parameters, results from extra simulations confirming the equilibration of the morphologies (investigation of effects of system starting configuration and system size), studying the effects of segregation strength, cross-link removal, and chain length on morphologies, and exploring the impact of the direction of the tensile deformations as well as examining their repeatability and relaxation (PDF)
>
> LML to PFL (MP4)
> CYL to PFL (MP4)
> PFL to LML (MP4)
> PFL to CYL (MP4)
> Stress relaxation strain video (MP4)
> Strain-composition morphology phase diagram video (MP4)

AUTHOR INFORMATION

Corresponding Author

Costas S. Patrickios − *Department of Chemistry, University of Cyprus, Nicosia 2109, Cyprus;* ⓞ orcid.org/0000-0001-8855-0370; Email: costasp@ucy.ac.cy

Authors

Dimitrios G. Tsalikis − *Department of Chemical Engineering, University of Patras, Patras 26504, Greece;* ⓞ orcid.org/0000-0002-6607-1528

Mihai Ciobanu − *Department of Chemistry, University of Cyprus, Nicosia 2109, Cyprus*

Yuji Higuchi − *Research Institute for Information Technology, Kyushu University, Fukuoka 819-0395, Japan;* ⓞ orcid.org/0000-0001-8759-3168

Complete contact information is available at:
https://pubs.acs.org/10.1021/acs.macromol.3c01392

■ DEDICATION

This work is dedicated to Prof. D. N. Theodorou of the National Technical University of Athens (NTUA), Greece, on the occasion of his 66th birthday.

■ REFERENCES

(1) Chen, D.; Kennedy, J. P.; Allen, A. J. Amphiphilic Networks. I. Network Synthesis by Copolymerization of Methacryloyl-Capped Polyisobutylene with 2-(Dimethylamino) Ethyl Methacrylate and Characterization of the Networks. *J. Macromol. Sci., Chem.* **1988**, *25*, 389−401.

(2) Weber, M.; Stadler, R. Hydrophilic-Hydrophobic Two-Component Polymer Networks: 1. Synthesis of Reactive Poly(ethylene oxide) Telechelics. *Polymer* **1988**, *29*, 1064−1070.

(3) *Amphiphilic Polymer Co-networks: Synthesis, Properties, Modelling and Applications*; Patrickios, C. S., Ed.; RSC: Cambridge, U.K., 2020.

(4) Patrickios, C. S.; Matyjaszewski, K. Amphiphilic Polymer Co-networks: 32 Years Old and Growing Stronger - A Perspective. *Polym. Int.* **2021**, *70*, 10−13.

(5) McLeod, K. R.; Tew, G. N. Microphase-Separated Thiol-Ene Conetworks from Telechelic Macromonomers with Asymmetric Molecular Weights. *Macromolecules* **2017**, *50*, 8042−8047.

(6) Apostolides, D. E.; Patrickios, C. S.; Sakai, T.; Guerre, M.; Lopez, G.; Améduri, B.; Ladmiral, V.; Simon, M.; Gradzielski, M.; Clemens, D.; Krumm, C.; Tiller, J. C.; Ernould, B.; Gohy, J.-F. Near-model Amphiphilic Polymer Conetworks Based on Four-arm Stars of Poly(vinylidene fluoride) and Poly(ethylene glycol): Synthesis and Characterization. *Macromolecules* **2018**, *51*, 2476−2488.

(7) Melodia, D.; Bhadra, A.; Lee, K.; Kuchel, R.; Kundu, D.; Corrigan, N.; Boyer, C. 3D Printed Solid Polymer Electrolytes with Bicontinuous Nanoscopic Domains for Ionic Liquid Conduction and Energy Storage. *Small* **2023**, 2206639.

(8) Sittko, I.; Kremser, K.; Roth, M.; Kuehne, S.; Stuhr, S.; Tiller, J. C. Amphiphilic Polymer conetworks with Defined Nanostructure and Tailored Swelling Behavior for Exploring the Activation of an Entrapped Lipase in Organic Solvents. *Polymer* **2015**, *64*, 122−129.

(9) Wang, H.; Jasensky, J.; Ulrich, N. W.; Cheng, J.; Huang, H.; Chen, Z.; He, C. Capsaicin-Inspired Thiol-Ene Terpolymer Networks Designed for Antibiofouling Coatings. *Langmuir* **2017**, *33*, 13689−13698.

(10) Malo de Molina, P.; Kafouris, D.; Patrickios, C. S.; Noirez, L.; Gradzielski, M. Amphiphilic Polymer Conetworks Studied by SANS: Effect of the Type of Solubilizate and Molecular Architecture on the Swollen Gel Structure. *Macromolecules* **2023**, *56*, 8323−8332.

(11) Chandel, A. K. S.; Nutan, B.; Raval, I. H.; Jewrajka, S. K. Self-Assembly of Partially Alkylated Dextran-graft-poly[(2-dimethylamino)ethyl methacrylate] Copolymer Facilitating Hydrophobic/Hydrophilic Drug Delivery and Improving Conetwork Hydrogel Properties. *Biomacromolecules* **2018**, *19*, 1142−1153.

(12) Guzman, G.; Nugay, T.; Nugay, I.; Nugay, N.; Kennedy, J.; Cakmak, M. High Strength Bimodal Amphiphilic Conetworks for Immunoisolation Membranes: Synthesis, Characterization, and Properties. *Macromolecules* **2015**, *48*, 6251−6262.

(13) Bomgardner, M. M. Making Better Contact Lenses. *Chemical & Engineering News*, 2017; Vol. 95, pp 29−33.

(14) Mutlu, Z.; Shams Es-haghi, S.; Cakmak, M. Recent Trends in Advanced Contact Lenses. *Adv. Healthcare Mater.* **2019**, *8*, 1801390.

(15) Moser, T.; Celma, C.; Lebert, A.; Charrault, E.; Brooke, R.; Murphy, P. J.; Browne, G.; Young, R.; Higgs, T.; Evans, D. Hydrophilic Organic Electrodes on Flexible Hydrogels. *ACS Appl. Mater. Interfaces* **2016**, *8*, 974−982.

(16) Patrickios, C. S. Thirty Years of Amphiphilic Polymer Co-networks, In *Amphiphilic Polymer Co-networks: Synthesis, Properties, Modelling and Applications*; Patrickios, C. S., Ed.; RSC: Cambridge, U.K., 2020; Chapter 1, pp 1−14.

(17) Kali, G.; Georgiou, T. K.; Iván, B.; Patrickios, C. S.; Loizou, E.; Thomann, Y.; Tiller, J. C. Synthesis and Characterization of Anionic Amphiphilic Model Conetworks Based on Methacrylic Acid and Methyl Methacrylate: Effects of Composition and Architecture. *Macromolecules* **2007**, *40*, 2192−2200.

(18) Triftaridou, A. I.; Vamvakaki, M.; Patrickios, C. S. Cationic Amphiphilic Model Networks Based on Symmetrical ABCBA Pentablock Terpolymers: Synthesis, Characterization and Modeling. *Biomacromolecules* **2007**, *8*, 1615−1623.

(19) Vamvakaki, M.; Patrickios, C. S.; Lindner, P.; Gradzielski, M. Amphiphilic Networks Based on Cross-Linked Star Polymers: A Small-Angle Neutron Scattering Study. *Langmuir* **2007**, *23*, 10433−10437.

(20) Kali, G.; Georgiou, T. K.; Iván, B.; Patrickios, C. S.; Loizou, E.; Thomann, Y.; Tiller, J. C. Synthesis and Characterization of Anionic Amphiphilic Model Conetworks of 2-Butyl-1-Octyl Methacrylate and Methacrylic Acid: Effects of Polymer Composition and Architecture. *Langmuir* **2007**, *23*, 10746−10755.

(21) Triftaridou, A. I.; Loizou, E.; Patrickios, C. S. Synthesis and Characterization of Amphiphilic Cationic Symmetrical ABCBA Pentablock Terpolymer Networks: Effect of Hydrophobic Content. *J. Polym. Sci., Part A: Polym. Chem.* **2008**, *46*, 4420−4432.

(22) Kafouris, D.; Gradzielski, M.; Patrickios, C. S. Semisegmented Amphiphilic Polymer Conetworks: Synthesis and Characterization. *Macromolecules* **2009**, *42*, 2972−2980.

(23) Hadjiantoniou, N. A.; Patrickios, C. S.; Thomann, Y.; Tiller, J. C. Amphiphilic Conetworks Based on End-Linked Multiblock Copolymers of Different Numbers of Blocks and Constant Molecular Weight and Composition. *Macromol. Chem. Phys.* **2009**, *210*, 942−950.

(24) Rikkou, M. D.; Loizou, E.; Porcar, L.; Butler, P.; Patrickios, C. S. Degradable, Amphiphilic End-linked Conetworks With Aqueous Degradation Rates Determined by Polymer Topology. *Macromolecules* **2009**, *42*, 9412−9421.

(25) Rikkou, M. D.; Loizou, E.; Patrickios, C. S.; Porcar, L. Structural Characterization of Amphiphilic Polymer Conetworks End-linked With the Optimal Amount of Cross-linker. *Eur. Polym. J.* **2010**, *46*, 441−449.

(26) Pafiti, K. S.; Loizou, E.; Patrickios, C. S.; Porcar, L. End-Linked Semifluorinated Amphiphilic Polymer Conetworks: Synthesis by Sequential Reversible Addition−Fragmentation Chain Transfer Polymerization and Characterization. *Macromolecules* **2010**, *43*, 5195−5204.

(27) Rikkou-Kalourkoti, M.; Kitiri, E. N.; Patrickios, C. S.; Leontidis, E.; Constantinou, M.; Constantinides, G.; Zhang, X. H.; Papadakis, C. M. Double-networks Based on Amphiphilic Cross-linked Star Block Copolymer First Conetworks and Randomly Cross-linked Hydrophilic Second Networks. *Macromolecules* **2016**, *49*, 1731−1742.

(28) Zhang, X.; Kyriakos, K.; Rikkou-Kalourkoti, M.; Kitiri, E. N.; Patrickios, C. S.; Papadakis, C. M. Amphiphilic Single and Double Networks: A Small-angle X-ray Scattering Investigation. *Colloid Polym. Sci.* **2016**, *294*, 1027−1036.

(29) Kitiri, E. N.; Patrickios, C. S.; Voutouri, C.; Stylianopoulos, T.; Hoffmann, I.; Schweins, R.; Gradzielski, M. Double-networks based on pH-responsive, amphiphilic "core-first" star first polymer conetworks prepared by sequential RAFT polymerization. *Polym. Chem.* **2017**, *8*, 245−259.

(30) Kitiri, E. N.; Varnava, C. K.; Patrickios, C. S.; Voutouri, C.; Stylianopoulos, T.; Gradzielski, M.; Hoffmann, I. Double-networks Based on Interconnected Amphiphilic "In-out" Star First Polymer Conetworks Prepared by RAFT Polymerization. *J. Polym. Sci., Part A: Polym. Chem.* **2018**, *56*, 2161−2174.

(31) Clarke, B. R.; Tew, G. N. Bottlebrush Amphiphilic Polymer Co-Networks. *Macromolecules* **2022**, *55*, 5131−5139.

(32) Huang, C.-S.; Yakunin, S.; Avaro, J.; Kang, X.; Bodnarchuk, M. I.; Liebi, M.; Sun, X.; Rossi, R. M.; Kovalenko, M. V.; Boesel, L. F. Amphiphilic Polymer Co-Network: A Versatile Matrix for Tailoring the Photonic Energy Transfer in Wearable Energy Harvesting Devices. *Adv. Energy Mater.* **2022**, *12*, 2200441.

(33) Wilhelm, S. A.; Maricanov, M.; Brandt, V.; Katzenberg, F.; Tiller, J. C. Amphiphilic Polymer Conetworks with Ideal and Nonideal Swelling Behavior Demonstrated by Small Angle X-ray Scattering. *Polymer* **2022**, *242*, 124582.

(34) Hagmann, K.; Bunk, C.; Böhme, F.; von Klitzing, R. Amphiphilic Polymer Conetwork Gel Films Based on Tetra-Poly(ethylene Glycol) and Tetra-Poly(ε-Caprolactone). *Polymers* **2022**, *14*, 2555.

(35) Anuradha; Das, A.; Pal, S.; Jewrajka, S. K. Physical, Electrochemical, and Solvent Permeation Properties of Amphiphilic Conetwork Membranes Formed through Interlinking of Poly-(vinylidene fluoride)-*Graft*-Poly[(2-dimethylamino)ethyl Methacrylate] with Telechelic Poly(ethylene glycol) and Small. Molecular Weight Cross-Linkers. *Langmuir* **2022**, *38*, 15340−15352.

(36) Ida, S.; Okuno, T.; Morimura, M.; Suzuki, K.; Takeshita, H.; Oyama, M.; Nakajima, K.; Kanaoka, S. Structure-Property Correlation of Crosslinked Domain Hydrogels Exhibiting Thermoresponsive Mechanical Toughening and Hybridization with Photoluminescent Carbon Dots. *Polym. Chem.* **2022**, *13*, 3479−3488.

(37) Velasquez, S. T. R.; Jang, D.; Jenkins, P.; Liu, P.; Yang, L.; Korley, L. T. J.; Bruns, N. Peptide-Reinforced Amphiphilic Polymer Conetworks. *Adv. Funct. Mater.* **2022**, *32*, 2207317.

(38) Apostolides, D. E.; Patrickios, C. S.; Simon, M.; Gradzielski, M.; Blanazs, A.; Mussault, C.; Marcellan, A.; Alexander, N.; Wesdemiotis, C. Model Dynamic Covalent Thermoresponsive Amphiphilic Polymer Co-networks Based on Acylhydrazone End-linked Tetronic T904 Star Block Copolymers. *Polym. Chem.* **2023**, *14*, 201−211.

(39) Kepola, E. J.; Loizou, E.; Patrickios, C. S.; Leontidis, E.; Voutouri, C.; Stylianopoulos, T.; Schweins, R.; Gradzielski, M.; Krumm, C.; Tiller, J. C.; Kushnir, M.; Wesdemiotis, C. Amphiphilic Polymer Conetworks Based on End-linked "Core-first" Star Block Copolymers: Structure Formation with Long-range Order. *ACS Macro Lett.* **2015**, *4*, 1163−1168.

(40) Hiroi, T.; Kondo, S.; Sakai, T.; Gilbert, E. P.; Han, Y.-S.; Kim, T.-H.; Shibayama, M. Fabrication and Structural Characterization of Module-Assembled Amphiphilic Conetwork Gels. *Macromolecules* **2016**, *49*, 4940−4947.

(41) Matsen, M. W. The Standard Gaussian Model for Block Copolymer Melts. *J. Phys.: Condens. Matter* **2002**, *14*, R21−R47.

(42) Schmid, F. Theoretical Approaches to Amphiphilic Polymer Co-Networks. In *Amphiphilic Polymer Co-Networks: Synthesis, Properties, Modelling and Applications*; Patrickios, C. S., Ed.; RSC: Cambridge, U.K., 2020; Chapter 11, pp 239−262.

(43) Vamvakaki, M.; Patrickios, C. S. Polyelectrolytic Amphiphilic Model Networks in Water: A Molecular Thermodynamic Theory for Their Microphase Separation. *J. Phys. Chem. B* **2001**, *105*, 4979−4986.

(44) Georgiou, T. K.; Vamvakaki, M.; Patrickios, C. S. Microphase Separation Under Constraints: A Molecular Thermodynamic Theory for Polyelectrolytic Amphiphilic Model Networks in Water. *Polymer* **2004**, *45*, 7341−7355.

(45) Karbarz, M.; Stojek, Z.; Patrickios, C. S. Microphase Separation in the Bulk in ABA Triblock Copolymer-Based Model Conetworks: Effects of Core Crowding and Loop Formation. *Macromol. Theory Simul.* **2013**, *22*, 323−334.

(46) Varnava, C. K.; Patrickios, C. S. Model Amphiphilic Polymer Conetworks in Water: Prediction of Their Ability for Oil Solubilization. *ACS Omega* **2019**, *4*, 4721−4738.

(47) Wang, G.; Müller, M. Phase Separation of Regular, Quasi-Two-Dimensional AB Copolymer Networks. *Macromolecules* **2022**, *55*, 1279−1294.

(48) Qi, S.; Zhou, J.; Schmid, F. Shear Modulus of an Irreversible Diblock Copolymer Network from Self-Consistent Field Theory. *Macromolecules* **2019**, *52*, 9569−9577.

(49) Evans, A. M.; Strauss, M. J.; Corcos, A. R.; Hirani, Z.; Ji, W.; Hamachi, L. S.; Aguilar-Enriquez, X.; Chavez, A. D.; Smith, B. J.; Dichtel, W. R. Two-Dimensional Polymers and Polymerizations. *Chem. Rev.* **2022**, *122*, 442−564.

(50) Hoogerbrugge, P. J.; Koelman, J. M. V. A. Simulating Microscopic Hydrodynamic Phenomena with Dissipative Particle Dynamics. *Europhys. Lett.* **1992**, *19*, 155−160.

(51) Groot, R. D.; Warren, P. B. Dissipative Particle Dynamics: Bridging the Gap between Atomistic and Mesoscopic Simulation. *J. Chem. Phys.* **1997**, *107*, 4423−4435.

(52) Groot, R. D.; Madden, T. J. Dynamic Simulation of Diblock Copolymer Microphase Separation. *J. Chem. Phys.* **1998**, *108*, 8713−8724.

(53) Español, P.; Warren, P. B. Perspective: Dissipative Particle Dynamics. *J. Chem. Phys.* **2017**, *146*, 150901.

(54) Plimpton, S. Fast Parallel Algorithms for Short-Range Molecular Dynamics. *J. Comput. Phys.* **1995**, *117*, 1−19.

(55) Thompson, A. P.; Aktulga, H. M.; Berger, R.; Bolintineanu, D. S.; Brown, W. M.; Crozier, P. S.; in 't Veld, P. J.; Kohlmeyer, A.; Moore, S. G.; Nguyen, T. D.; Shan, R.; Stevens, M. J.; Tranchida, J.; Trott, C.; Plimpton, S. J. LAMMPS A Flexible Simulation Tool for Particle-based Materials Modeling at the Atomic, Meso, and Continuum Scales. *Comput. Phys. Commun.* **2022**, *271*, 108171.

(56) Yeh, I.-C.; Andzelm, J. W.; Rutledge, G. C. Mechanical and Structural Characterization of Semicrystalline Polyethylene under Tensile Deformation by Molecular Dynamics Simulations. *Macromolecules* **2015**, *48*, 4228−4239.

(57) Jabbari-Farouji, S.; Rottler, J.; Lame, O.; Makke, A.; Perez, M.; Barrat, J.-L. Plastic Deformation Mechanisms of Semicrystalline and Amorphous Polymers. *ACS Macro Lett.* **2015**, *4*, 147−150.

(58) Higuchi, Y.; Kubo, M. Coarse-grained Molecular Dynamics Simulation of the Void Growth Process in the Block Structure of Semicrystalline Polymers. *Modell. Simul. Mater. Sci. Eng.* **2016**, *24*, 055006.

(59) Higuchi, Y.; Kubo, M. Deformation and Fracture Processes of a Lamellar Structure in Polyethylene at the Molecular Level by a Coarse-Grained Molecular Dynamics Simulation. *Macromolecules* **2017**, *50*, 3690−3702.

(60) Higuchi, Y. Fracture Processes of Crystalline Polymers Using Coarse-grained Molecular Dynamics Simulations. *Polym. J.* **2018**, *50*, 579−588.

(61) Higuchi, Y. Stress Transmitters at the Molecular Level in the Deformation and Fracture Processes of the Lamellar Structure of Polyethylene via Coarse-Grained Molecular Dynamics Simulations. *Macromolecules* **2019**, *52*, 6201−6212.

(62) Higuchi, Y. Coarse-grained Molecular Dynamics Simulations of Void Generation and Growth Processes in the Fracture of the Lamellar Structure of Polyethylene. *Phys. Rev. E* **2021**, *103*, 042502.

(63) Jang, S. S.; Goddard, W. A.; Kalani, M. Y. S. Mechanical and Transport Properties of the Poly(ethylene oxide)-Poly(acrylic acid) Double Network Hydrogel from Molecular Dynamic Simulations. *J. Phys. Chem. B* **2007**, *111*, 1729−1737.

(64) Higuchi, Y.; Saito, K.; Sakai, T.; Gong, J. P.; Kubo, M. Fracture Process of Double-Network Gels by Coarse-Grained Molecular Dynamics Simulation. *Macromolecules* **2018**, *51*, 3075−3087.

(65) Zhang, M.; Zhang, D.; Chen, H.; Zhang, Y.; Liu, Y.; Ren, B.; Zheng, J. A Multiscale Polymerization Framework Towards Network Structure and Fracture of Double-network Hydrogels. *npj Comput. Mater.* **2021**, *7*, 39.

(66) Aguilera-Mercado, B. M.; Cohen, C.; Escobedo, F. A. Sawtooth Tensile Response of Model Semiflexible and Block Copolymer Elastomers. *Macromolecules* **2014**, *47*, 840−850.

(67) Nowak, C.; Escobedo, F. A. Tuning the Sawtooth Tensile Response and Toughness of Multiblock Copolymer Diamond Networks. *Macromolecules* **2016**, *49*, 6711−6721.

(68) Nowak, C.; Escobedo, F. A. Optimizing the Network Topology of Block Copolymer Liquid Crystal Elastomers for Enhanced Extensibility and Toughness. *Phys. Rev. Mater.* **2017**, *1*, 035601.

(69) Nowak, C.; Escobedo, F. A. Effect of Block Immiscibility on Strain-Induced Microphase Segregation and Crystallization of Model Block Copolymer Elastomers. *Macromolecules* **2018**, *51*, 5685−5693.

(70) Wakabayashi, R.; Imatani, R.; Katsuya, M.; Higuchi, Y.; Noguchi, H.; Kamiya, N.; Goto, M. Hydrophobic Immiscibility Controls Self-sorting or Co-assembly of Peptide Amphiphiles. *Chem. Commun.* **2022**, *58*, 585−588.

(71) Ma, S.; Hu, Y.; Wang, R. Self-Assembly of Polymer Tethered Molecular Nanoparticle Shape Amphiphiles in Selective Solvents. *Macromolecules* **2015**, *48*, 3112−3120.

(72) Nakagawa, K. M.; Noguchi, H. Morphological Changes of Amphiphilic Molecular Assemblies Induced by Chemical Reactions. *Soft Matter* **2015**, *11*, 1403−1411.

(73) Berezkin, A. V.; Papadakis, C. M.; Potemkin, I. I. Vertical Domain Orientation in Cylinder-Forming Diblock Copolymer Films upon Solvent Vapor Annealing. *Macromolecules* **2016**, *49*, 415−424.

(74) Huang, H.; Alexander-Katz, A. Dissipative Particle Dynamics for Directed Self-assembly of Block Copolymers. *J. Chem. Phys.* **2019**, *151*, 154905.

(75) Matsen, M. W.; Schick, M. Microphase Separation in Starblock Copolymer Melts. *Macromolecules* **1994**, *27*, 6761−6767.

(76) Xu, Y.; Feng, J.; Liu, H.; Hu, Y. Microphase Separation of Star-diblock Copolymer Melts Studied by Dissipative Particle Dynamics Simulation. *Mol. Simul.* **2006**, *32*, 375−383.

(77) Matsen, M. W. Effect of Architecture on the Phase Behavior of AB-Type Block Copolymer Melts. *Macromolecules* **2012**, *45*, 2161−2165.

(78) Liu, R.; Sun, Z.; Huang, H.; Johnson, J. A.; Alexander-Katz, A.; Ross, C. A. Experimental and Computational Evaluation of Self-Assembled Morphologies in Diblock Janus Bottlebrush Copolymers. *Nano Lett.* **2023**, *23*, 177−182.

(79) Gârlea, I. C.; Jaramillo-Cano, D.; Likos, C. N. Self-organization of Gel Networks Formed by Block Copolymer Stars. *Soft Matter* **2019**, *15*, 3527−3540.

(80) Jaramillo-Cano, D.; Camargo, M.; Likos, C. N.; Gârlea, I. C. Dynamical Properties of Concentrated Suspensions of Block Copolymer Stars in Shear Flow. *Macromolecules* **2020**, *53*, 10015−10027.

(81) Rubinstein, M.; Colby, R. H. *Polymer Physics*; Oxford University Press: New York, 2003; pp 51−54.

(82) Mortensen, K.; Annaka, M. Stretching PEO-PPO Type of Star Block Copolymer Gels: Rheology and Small-Angle Scattering. *ACS Macro Lett.* **2018**, *7*, 1438−1442.

(83) Caccavo, D.; Cascone, S.; Lamberti, G.; Barba, A. A. Hydrogels: Experimental Characterization and Mathematical Modelling of Their Mechanical and Diffusive Behaviour. *Chem. Soc. Rev.* **2018**, *47*, 2357−2373.

(84) Glynos, E.; Pantazidis, C.; Sakellariou, G. Designing All-Polymer Nanostructured Solid Electrolytes: Advances and Prospects. *ACS Omega* **2020**, *5*, 2531−2540.

(85) Schmid, F. Self-Consistent Field Approach for Cross-Linked Copolymer Materials. *Phys. Rev. Lett.* **2013**, *111*, 028303.

(86) Panyukov, S.; Rubinstein, M. Stress-Induced Ordering in Microphase-Separated Multicomponent Networks. *Macromolecules* **1996**, *29*, 8220−8230.

(87) Sakurai, S.; Aida, S.; Okamoto, S.; Ono, T.; Imaizumi, K.; Nomura, S. Preferential Orientation of Lamellar Microdomains Induced by Uniaxial Stretching of Cross-Linked Polystyrene-*block*-polybutadiene-*block*-polystyrene Triblock Copolymer. *Macromolecules* **2001**, *34*, 3672−3678.